Theoretical Chemistry Accounts (2019) 138:107
https://doi.org/10.1007/s00214-019-2498-y

REGULAR ARTICLE

Methane functionalization by an Ir(III) catalyst supported on a metal–organic framework: an alternative explanation of steric confinement effects

Bo Yang[1] · Xin-Ping Wu[1] · Laura Gagliardi[1] · Donald G. Truhlar[1]

Received: 19 June 2019 / Accepted: 16 August 2019 / Published online: 24 August 2019

Abstract
A highly selective Ir catalyst supported on the metal–organic framework (MOF) UiO-67 for the catalytic borylation of methane has recently been synthesized. The high chemoselectivity of the catalyst toward monoborylated methane (CH_3Bpin, Bpin = pinacolborane) instead of diborylated methane (CH_2Bpin_2) was speculated to be caused by the steric confinement of MOF UiO-67. In this study, we applied quantum mechanical methods to determine: (1) the steric effect of the UiO-67 framework in promoting the chemoselectivity of the Ir catalyst toward CH_3Bpin and (2) the borylation mechanisms over the Ir catalyst supported on UiO-67. Our results show that UiO-67 framework sterically obstructs the diffusion of the larger CH_2Bpin_2 molecule within the MOF while allowing the smaller CH_3Bpin molecule to pass through with little energy penalty. The diffusion of CH_2Bpin_2 from the tetrahedral pore to the tetragonal pyramidal pore within modified UiO-67 with coordinated $Ir(Bpin)_3$ complex has an estimated barrier of 24.7 kcal/mol and is 14.2 kcal/mol higher than the diffusion of CH_3Bpin. The electronic and steric effects of the support at the Ir catalytic center are much smaller than this confinement effect on diffusion, and the catalytic center behaves similarly to the homogeneous Ir catalyst. We determined an overall free energy of activation of 34.6 kcal/mol for the CH_4 borylation reaction using the Ir(III) catalyst. We also determined that the turnover-determining step for the catalytic methane borylation is the isomerization of seven-coordinated Ir(V) complex instead of the commonly assumed C–H bond activation by oxidative addition.

Keywords Methane borylation · Ir(III) complexes · Steric confinement effect · Metal–organic framework · Heterogeneous catalysis · Density functional theory

1 Introduction

There is an increasing demand for the direct functionalization of light alkanes (C1–C4) to produce higher-value chemicals, such as olefins and alcohols. Methane (CH_4) is one of the most important potential feedstocks due to its high concentration in natural gas, but it is the most challenging alkane for functionalization due to its strong C–H bonds [1–3]. Transition-metal-catalyzed methane borylation with bis(pinacolborane) (i.e., B_2pin_2) as the activating reagent (Fig. 1) is a promising method for methane activation under mild reaction conditions [3, 4]. However, conventional organometallic catalysts exhibit low chemoselectivity toward monoborylated methane (CH_3Bpin) (reaction R1), which is the desired product for producing liquid fuel (i.e., CH_3OH); instead, they yield diborylated methane (CH_2Bpin_2) (reaction R2) as the main product. The selectivity toward the

Electronic supplementary material The online version of this article (https://doi.org/10.1007/s00214-019-2498-y) contains supplementary material, which is available to authorized users.

✉ Bo Yang
yang3227@umn.edu

✉ Laura Gagliardi
gagliardi@umn.edu
http://www1.chem.umn.edu/groups/gagliardi/

✉ Donald G. Truhlar
truhlar@umn.edu
http://truhlar.chem.umn.edu

[1] Department of Chemistry, Inorganometallic Catalyst Design Center, Chemical Theory Center, and Minnesota Supercomputing Institute, University of Minnesota, 207 Pleasant Street SE, Minneapolis, MN 55455-0431, USA

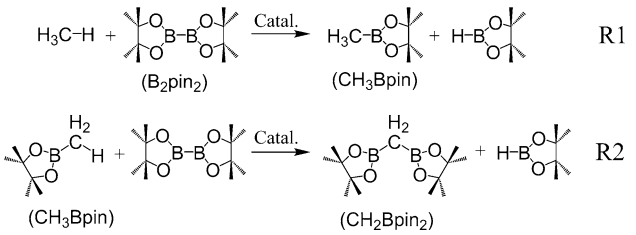

Fig. 1 (R1) Catalytic CH_4 borylation to give CH_3Bpin and the subsequent; (R2) CH_3Bpin borylation over the same catalyst

Table 1 Lattice parameters (Å) for pristine UiO-67 and modified UiO-67 with coordinated $Ir(Bpin)_3$ complex

	a	b	c
UiO-67 (experiment [27])	26.8809	26.8809	26.8809
UiO-67 (DFT)	26.8898	26.8898	26.8898
UiO-67-Ir(Bpin)$_3$ (DFT)	26.8210	26.9049	26.8460

Computed (DFT) lattice parameters were acquired using the PBEsol functional [25] as implemented in the *VASP* package [21–24]

diborylated species is due to the C–H bonds being more reactive in CH_3Bpin than in CH_4 [5].

Metal–organic frameworks (MOFs) provide a promising platform for heterogenization and stabilization of homogeneous organometallic catalysts with high activity and selectivity [6–17]. Universitetet i Oslo-67 (UiO-67), is a MOF composed of Zr_6 inorganic nodes ($Zr_6(\mu_3\text{-}O)_4(\mu_3\text{-}OH)_4$) and 4,4′-biphenyl dicarboxylate (bpdc) linkers, and it is a particularly suitable catalyst support because of its high stability. Zhang et al. [5] have recently reported a catalyst, called UiO-67-Mix-Ir, that involves Ir(III) complexes supported on MOF UiO-67 through 1,10-phenanthroline-3,8-dicarboxylate (phendc) linker groups. The phendc linker is used in replacement of the bpdc linker for tethering the Ir(III) complex [5]. The newly synthesized complex was found to have excellent chemoselectivity (> 99%) to produce exclusively monoborylated methane, and the high selectivity was attributed to steric confinement effects of the microporous MOF UiO-67 [5]. The catalytic reaction on UiO-67 has both higher yield and higher selectivity for monoborylated methane than does the homogeneously catalyzed reaction [5, 18, 19], but the nature of the steric effect was not ascertained.

In the present study, we use density functional theory (DFT) calculations on model compounds to determine the selectivity of various UiO-67-supported Ir catalysts as potential active centers for the methane borylation reaction and to elucidate the confinement effect.

2 Computational methods

There are three kinds of calculations: (i) periodic calculations, (ii) octahedral model and triangular prism model (tpm) calculations, and (iii) calculations on the small complexes that do not involve any bpdc linkers. Calculations of types i and ii are electronic energies (including nuclear repulsion) in the gas phase. Calculations of type iii are gas-phase free energies with two exceptions in the borylation mechanism subsection: (1) In some cases we specify "electronic energy" or "electronic activation barrier" so that we can compare the energies with the *CP2K* results for larger cluster models. (2) In some cases we include solvation effects in the free energies by adding the free energy of solvation calculated by the SMD continuum model [20] with the gas-phase optimized geometries.

All periodic model calculations were performed using the *Vienna* Ab initio *simulation* package (*VASP*) [21–24]. We used the PBEsol density functional [25] with the PAW potential [26] and an energy cutoff of 500 eV for the periodic calculations. For pristine UiO-67, we calculated lattice parameters of $a = b = c = 26.890$ Å (Table 1), which is in good agreement with the experimentally measured value 26.881 Å [27], and hence, it validates the method.

The triangular prism models and octahedral models have bpdc linkers and Zr_6 nodes. They were calculated with the *CP2K* program [28]. For these calculations, formates were used as capping groups for the Zr_6 nodes at places where the bpdc linkers were removed to make the cluster model as a truncated version of periodic crystal. The C atoms in the capping formate groups were fixed at their positions in the optimized periodic structure. The octahedral model geometries were optimized using the PBE [29] functional. The DZVP-MOLOPT basis set, a plane wave cutoff energy of 360 Ry, and pseudopotentials for core electrons (as formulated by Geodecker et al. [30]) were used for all atoms. The diffusion processes of the CH_3Bpin and the CH_2Bpin_2 molecules in the triangular prism model were calculated using the *CP2K* program in the same way with the addition of the D3 damped dispersion terms of Grimme et al. [31].

The small complexes that do not involve any bpdc linkers were calculated using unrestricted DFT as implemented in the *Gaussian 16* [32] program. These calculations used the M06-L functional [33], which shows high accuracy for transition metal chemistry [34, 35]. We used the def2-TZVP basis set [36, 37] for the Ir, B, N, O atoms and for C and H atoms that are directly bonded to the Ir atom. The def2-SVP basis set [36, 37] was used for other atoms. We verified that for all molecules, the singlet spin state is lower in energy than the triplet and quintet spin states, and the singlets converged to closed-shell configurations with no spin contamination. Transition structures were optimized using the eigenmode-following method by using the *Gaussian* keyword TS. We verified that all frequencies of stable species are real, and for each transition structure we verified that there is only

one imaginary frequency. For each optimized geometry, we computed the Gibbs free energy (G) at 298.15 K. To obtain G, we used the FREQ [38] program to generate a vibrational frequency scaling factor of 0.976, and real frequencies below 100 cm^{-1} are raised to 100 cm^{-1} to simulate low-frequency anharmonic effects [39].

3 Results and discussion

3.1 Steric effect of the UiO-67 framework

We first consider the triangular prism model (tpm-UiO-67) in Fig. 2 for examining the UiO-67 framework confinement on CH_3Bpin and CH_2Bpin_2 transport. This model was extracted from a geometry-optimized periodic structure of pristine UiO-67, and replication of this triangular prism model in space gives the UiO-67 periodic structure. Details of the geometry optimization are reported in the Computational Methods section. The triangular prism model includes 6 Zr_6 nodes and 11 bpdc linkers. Formates were used as capping groups for the Zr_6 nodes at places where the bpdc linkers were removed and the C atom in each formate is fixed at the position of the corresponding carbon in the optimized periodic structure.

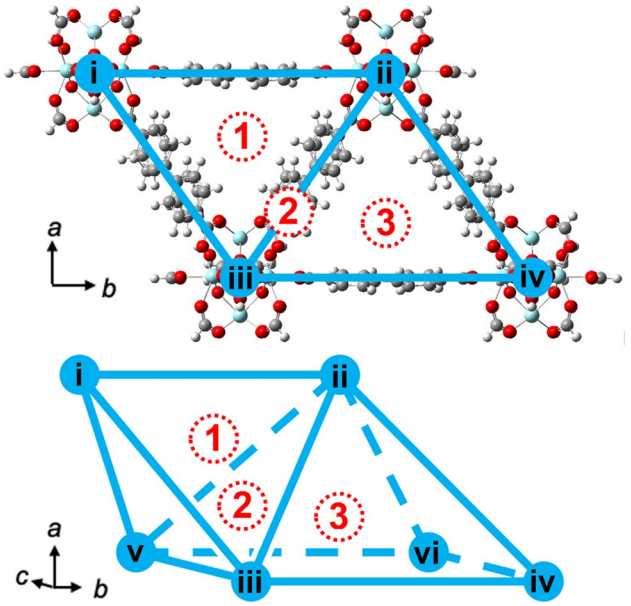

Fig. 2 Triangular prism model of UiO-67 (tpm-UiO-67) with six Zr_6 nodes (labeled i to vi) showing the tetrahedral pore (position 1, surrounded by nodes i, ii, iii, and v) and the tetragonal pyramidal pore (position 3, surrounded by nodes iii, iv, v, and vi, which form a square, and node ii at the apex). The pores are connected by the triangular aperture (position 2, surrounded by nodes ii, iii, and v). C atoms are shown in gray, H in white, O in red, and Zr in cyan

As shown in Fig. 2, the triangular prism model consists of two distinctive pore structures, namely the tetrahedral pore and the tetragonal pyramidal pore; the centers of the pores are marked, respectively, as positions 1 and 3 in Fig. 2. A triangular aperture marked as position 2 connects the two kinds of pores. For a molecule in the MOF to migrate to the surface of the MOF (so it can be released), it is necessary for it to pass between the two pores along a path like the path from 1 to 2 to 3.

Both CH_3Bpin and CH_2Bpin_2 molecules can be fitted without steric strain into both the tetrahedral pore and the tetragonal pyramidal pore. We calculated the energy profile for diffusion of a CH_3Bpin or a CH_2Bpin_2 from position 1 to 2 to 3. Activation barriers for the diffusion processes were estimated by the following steps: (i) Equilibrium structures were optimized with the CH_3Bpin or the CH_2Bpin_2 molecule at positions 1, 2, and 3 (shown in Fig. 2) and with the C atoms of the capping formates fixed at their positions in the periodic structure; (ii) five intermediate geometries with the CH_3Bpin or the CH_2Bpin_2 molecule between positions 1 and 2 and between positions 2 and 3 were constructed using linear interpolation of the C atom coordinate of the $–CH_3$ or $–CH_2–$ group that binds with Bpin groups; (iii) partial geometry optimization was performed on each intermediate with C coordinates of the $–CH_3$ or $–CH_2–$ group that binds with Bpin groups fixed with respect to the fixed C atoms of the capping formates; (iv) the highest energy of the intermediate structures was used as an approximation to the barrier height. The results for CH_3Bpin are connected by red lines in Fig. 3, and they show a rate-determining barrier (highest-energy transition structure minus lowest-energy equilibrium structure) of 6.3 kcal/mol. The results for CH_2Bpin_2 are joined by black lines in Fig. 3, and they

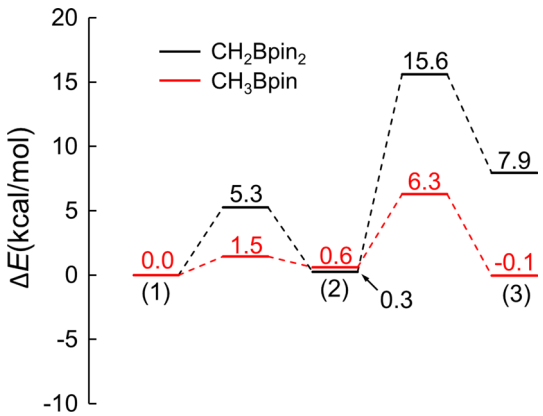

Fig. 3 Energy profiles for CH_3Bpin and CH_2Bpin_2 transport in UiO-67. Positions 1, 2, and 3 represent equilibrium geometries in the tetrahedral pore, the triangular window, and the tetragonal pyramidal pore of the tpm-UiO-67 model, respectively. Electronic energy for each intermediate was calculated using the *CP2K* program [28] with the PBE + D3 functional [29, 31]

show a rate-determining barrier of 15.6 kcal/mol. Detailed results are provided in the *Electronic Supplementary Material* (ESM).

In the 2 → 3 transition structure for CH_2Bpin_2, we see bending and twisting of the bpdc linker groups, whereas only minor deformation of the linkers is observed for the CH_3Bpin case. We conclude from this that the comparatively higher barrier of the CH_2Bpin_2 transport is mainly due to noncovalent steric interactions between the CH_2Bpin_2 molecule and the bpdc linkers. Figure S1 in the ESM shows the optimized 2 → 3 transition structure with the bent bpdc linker groups.

The higher barrier for moving CH_3Bpin and CH_2Bpin_2 through the UiO-67 framework implies that CH_2Bpin_2 will have a much smaller diffusion rate than CH_3Bpin within UiO-67. This trend should not change (however the barrier difference might vary) when the aperture size of the framework decreases due to the existence of modified linkers and tethered catalysts. Therefore, assuming that both CH_3Bpin and CH_2Bpin_2 were generated through the borylation reaction over the Ir catalyst anchored to the modified UiO-67, it will be comparatively easier for CH_3Bpin to diffuse out of the framework, and the Ir catalyst supported on UiO-67 will experimentally appear to have high selectivity toward CH_3Bpin. This hypothesis is further tested using the triangular prism model of the modified UiO-67 with a coordinated $Ir(Bpin)_3$ complex (tpm-UiO-67-Ir).

A schematic representation of the tpm-UiO-67-Ir model is given in Fig. 4. Using the same procedure as for the construction of the tpm-UiO-67 model, the tpm-UiO-67-Ir model was extracted from a geometry-optimized periodic structure of modified UiO-67 with a coordinated $Ir(Bpin)_3$ complex. Details of the geometry optimization for modified UiO-67 with coordinated $Ir(Bpin)_3$ complex (UiO-67-$Ir(Bpin)_3$) are reported in the Computational Methods section. In comparison with the tpm-UiO-67 model, the tpm-UiO-67-Ir has one Ir center between Zr_6 nodes iii and v with three attached Bpin groups. The bpdc linker between Zr_6 nodes iii and v in the tpm-UiO-67 model is replaced with a phendc linker to provide the anchoring point for the Ir atom.

The diffusion of CH_3Bpin and CH_2Bpin_2 passing through the tpm-UiO-67-Ir model individually from position 4 to 5 to 6 is simulated in the same manner as our previous calculations with the tpm-UiO-67 model. The corresponding energy profiles for the diffusion processes are provided in Fig. 5 with the results for CH_3Bpin and CH_2Bpin_2 connected, respectively, by red and black lines. The estimated rate-determining barrier for CH_3Bpin transport in tpm-UiO-67-Ir is 10.5 kcal/mol and is 4.2 kcal/mol higher than its transport in tpm-UiO-67. Moreover, as anticipated, the steric confinement effect in the tpm-UiO-67-Ir compared to that of the tpm-UiO-67 is increased to a greater extent for the CH_2Bpin_2 diffusion process than for the CH_3Bpin one. In particular, we find an increase of 9.1 kcal/mol in the rate-determining barrier (from 15.6 to 24.7 kcal/mol) for the diffusion of CH_2Bpin_2 when tpm-UiO-67 is replaced by the more sterically crowded tpm-UiO-67-Ir. This confirms that the modified UiO-67 framework with coordinated $Ir(Bpin)_3$ complex provides higher steric confinement effect than the pristine UiO-67 in the CH_3Bpin and CH_2Bpin_2 diffusion processes. Comparing CH_3Bpin with CH_2Bpin_2, the diffusion of the latter in the framework is more strongly affected by the confinement effect than the diffusion of the former.

Note, the Ir loading in the tpm-UiO-67-Ir model is considerably lower than that of the experimental system reported by Zhang et al. [5]. According to the reported experimental procedures, about 33% of the bpdc linkers were replaced with phendc linkers in the modified UiO-67 [5]. Therefore, for each tpm-UiO-67 fragment, there would be around 3-to-4 Ir active centers experimentally instead of 1 as in the tpm-UiO-67-Ir model. We believe that a further increase of the Ir

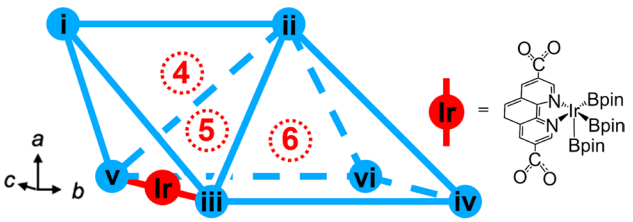

Fig. 4 Triangular prism model of modified UiO-67 with coordinated $Ir(Bpin)_3$ complex (tpm-UiO-67-Ir). For the clarity of the figure, we use red circle (labeled Ir) to represent 1 Ir atom bound with 3 Bpin groups. We use red and blue sticks to represent, respectively, the phendc and the bpdc linkers. Six Zr_6 nodes (blue circles labeled i to vi) showing the tetrahedral pore (position 4), the tetragonal pyramidal pore (position 6), and the triangular aperture (position 5). Optimized coordinates for tpm-UiO-67-Ir are provided in the ESM

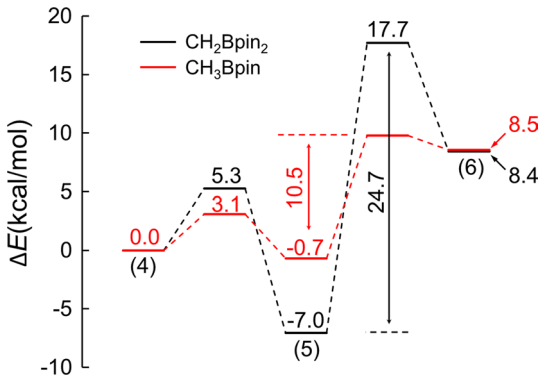

Fig. 5 Energy profiles for CH_3Bpin and CH_2Bpin_2 transport in tpm-UiO-67-Ir. Positions 4, 5, and 6 represent equilibrium geometries in the tetrahedral pore, the triangular window, and the tetragonal pyramidal pore of the tpm-UiO-67-Ir model, respectively. Electronic energy for each intermediate was calculated using the *CP2K* program [28] with the PBE + D3 functional [29, 31]

loading from 1 per tpm-UiO-67 model to 2 or 3 would result in an even higher diffusion barrier than 24.7 kcal/mol for CH_2Bpin_2 which would further lower its diffusion rate inside the framework. And as discussed earlier, the diffusion of the smaller CH_3Bpin molecule inside the MOF suffers less energy penalty from the increasing steric congestion, so the CH_3Bpin molecule would still be able to pass through the framework with higher Ir loadings. Due to the large amount of possible Ir binding-position combinations and the lack of experimental information on local catalyst structures, simulations of CH_3Bpin and CH_2Bpin_2 diffusions in models with 2 or more Ir centers are not performed in the current study.

We also note that the trapped CH_2Bpin_2 molecule in the modified MOF UiO-67 will not cause permanent congestion of the framework because the CH_2Bpin_2 molecule can be dissociated into CH_2Bpin and Bpin by a nearby tethered Ir center to give Ir(CH_2Bpin)(Bpin) and consequently free up the diffusion path of the framework. Details regarding the CH_2Bpin_2 dissociation reaction will be discussed in the "Further analyses of the chemoselectivity of the Ir-decorated UiO-67 catalyst" subsection. In addition, we will discuss the possible situation in which the reaction pathway of reaction R2 is blocked due to the steric confinement of the modified UiO-67 framework, which is another possible cause for the experimentally observed chemoselectivity of the UiO-67-supported Ir catalyst. However, our calculations do not show any evidence for such steric confinement effect of the framework at the Ir center.

3.2 Methane borylation catalyzed by Ir-decorated UiO-67

3.2.1 Relative stability of Ir(III) species

Experimentally, the Ir catalyst supported on UiO-67 was synthesized by first adding modified UiO-67 to a [Ir(COD)(μ-Cl)]$_2$ (COD = 1,5-cyclooctadiene) solution that was then reacted with B_2pin_2 molecules [5]. Based on this experimental procedure, we propose four possible Ir(III) complexes as potential active species for catalyzing the methane borylation reaction: (**a**) (phen)Ir(Bpin)$_3$, (**b**) *eq*-(phen)Ir(Bpin)$_2$Cl, (**c**) *axi*-(phen)Ir(Bpin)$_2$Cl, and (**d**) (phen)Ir(Bpin)$_2^+$; the structures are given in Fig. 6. In calculations on these complexes, the 1,10-phenanthroline (phen) ligand is used in replacement of the MOF support for simplicity and, as will be discussed below, has only a minor effect on the reactivity of the catalyst.

The stability of these complexes is evaluated relative to complex **a** as follows:

$$\Delta E(\mathbf{a}) = 0, \tag{1}$$

$$\Delta E(\mathbf{b}) = E(\mathbf{b}) + E\left(B_2pin_2\right) - E(\mathbf{a}) - E(\mathrm{ClBpin}), \tag{2}$$

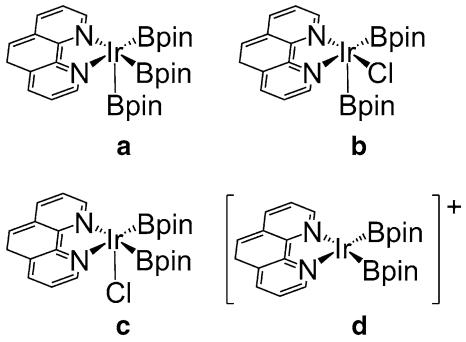

Fig. 6 Ir(III) complexes: **a** (phen)Ir(Bpin)$_3$, **b** *eq*-(phen)Ir(Bpin)$_2$Cl, **c** *axi*-(phen)Ir(Bpin)$_2$Cl, **d** (phen)Ir(Bpin)$_2^+$ cation

Table 2 Relative electronic energies (kcal/mol) for complexes **a**, **b**, **c** and **d**

	a	**b**	**c**	**d**
ΔE	0.0	7.1	36.8	132.7

Energies were acquired using the M06-L functional [33] as implemented in the *Gaussian 16* program [32]

$$\Delta E(\mathbf{c}) = E(\mathbf{c}) + E\left(B_2pin_2\right) - E(\mathbf{a}) - E(\mathrm{ClBpin}), \tag{3}$$

$$\Delta E(\mathbf{d}) = E(\mathbf{d}) + \Delta E(\mathbf{b}) - E(\mathbf{b}) + E(\mathrm{Cl}^-), \tag{4}$$

where $\Delta E(i)(i = \mathbf{a}, \mathbf{b}, \mathbf{c}, \mathbf{d})$ is the relative energy, and $E(j)\left(j = \mathbf{a}, \mathbf{b}, \mathbf{c}, \mathbf{d}, B_2pin_2, \mathrm{ClBpin}, \mathrm{Cl}^-\right)$ denotes the DFT energy of the corresponding molecule or ion. Table 2 shows the relative stability of the complexes. We see that complex **a** has the lowest energy.

3.2.2 Electronic effect of the UiO-67 framework

The relative stability of complexes **a**, **b**, and **c** was further tested using three larger models to be called the octahedral models: **oct-a**, **oct-b**, and **oct-c**.

The **oct-a** model is shown in Fig. 7; it was extracted from a DFT-optimized periodic structure, UiO-67-Ir(Bpin)$_3$, and formate groups were added to cap the Zr_6 nodes at places where the bpdc linkers were removed. (Details of the periodic calculations are in the Computational Methods section.) Models **oct-b** and **oct-c** are prepared by replacing one of the Bpin groups in **oct-a** with a Cl group to, respectively, reproduce the Ir-centered bonding motifs as in complexes **b** and **c**.

Geometry optimizations were performed for the octahedral models with C atoms of capping formates fixed at the corresponding C positions of the carboxylate groups of the replaced bpdc linkers. The relative energies of the three octahedral models are calculated based on Eqs. 1–3 with $E(\mathbf{a})$, $E(\mathbf{b})$, and $E(\mathbf{c})$ replaced by E(**oct-a**), E(**oct-b**), and E(**oct-c**), respectively; results are in Table 3. Comparing

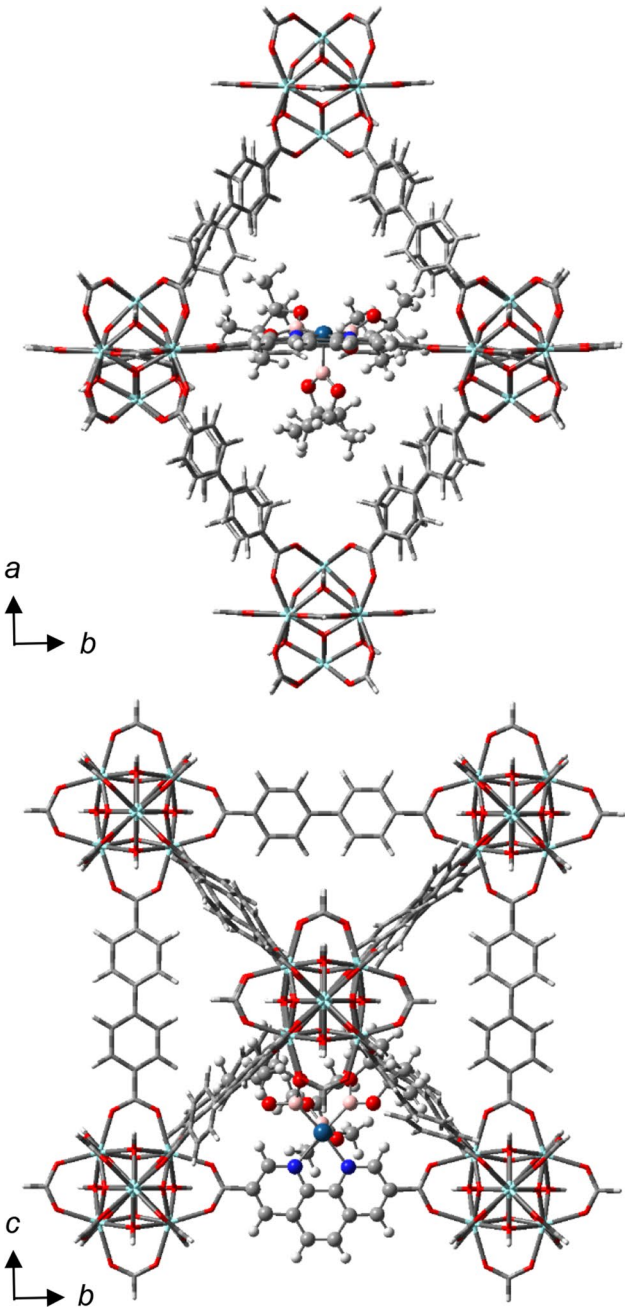

Fig. 7 $Ir(Bpin)_3$ complex (**oct-a**) supported on UiO-67 viewed along the *c* and *a* directions (C atoms in gray, H in white, O in red, B in pink, N in blue, and Ir in teal, with the $Ir(Bpin)_3$ complex and part of the phendc linker shown as balls and sticks)

Table 3 Relative energies (kcal/mol) for octahedral models

	oct-a	oct-b	oct-c
ΔE	0.0	6.4	41.2

Energies were acquired using the PBE functional [29] as implemented in the *CP2K* program [28]

Table 3 with Table 2, we see the same trend of energies for the three Ir(III) complexes, and this suggests a negligible effect of the framework on the Ir(III) complexes.

To further verify the negligible effect of the framework, Charge Model 5 (CM5) charge analyses [40] were performed for complexes **a**, **e**, and **f** with structures shown in Fig. 8, where Zr_6 denotes a node. The latter two complexes were made by appending various functional groups to the third and eighth C positions of the 1,10-phenanthroline ligand. The CM5 charges of the Ir atoms in complexes **a**, **e**, and **f** are, respectively, 0.591, 0.597, and 0.609. The small charge differences observed between the three complexes suggest that the UiO-67 framework would have no significant electronic effect on the Ir catalytic active center. We therefore used complexes **a** and **b** without the UiO-67 framework to study the mechanism of methane borylation.

3.2.3 Methane activation over Ir(III) species

Because complexes **a** and **b** have similar relative energies (Tables 2 and 3), we assume they are both accessible under the experimental [5] 150 °C reaction conditions, and we consider both of them in studying the catalytic mechanisms. Two activation mechanisms were considered: (1) oxidative addition of methane to give Ir-hydride and Ir-methyl bonds, and (2) σ-bond metathesis to give an Ir-hydride intermediate with CH_3Bpin or a methyl intermediate with HBpin. All attempts at optimizing a transition state geometry of the σ-bond metathesis reaction gave the transition state that connects to the reactant and product of the oxidative addition reaction instead. Therefore, we consider the oxidative addition in the rest of the article.

For complex **a**, the oxidative addition reaction (Fig. 9) gives a free energy of activation of 29 kcal/mol for methane activation. The product of oxidative addition is a seven-coordinated (phen)Ir(H)(methyl)$(Bpin)_3$ complex (**g** in Fig. 10) with an axial methyl group and an equatorial hydride group.

For complex **b**, the oxidative addition of methane requires a minimum free energy of activation of 40 kcal/mol,

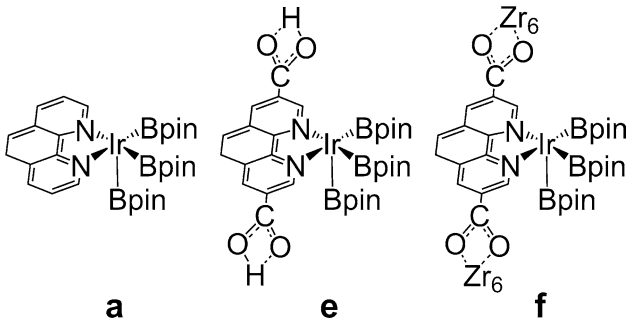

Fig. 8 The (phen)$Ir(Bpin)_3$ complex (**a**) and two modifications in which two H atoms are replaced by (**e**) COOH or (**f**) $(COO)Zr_6$

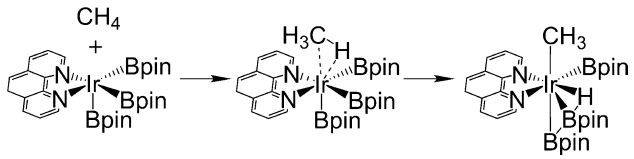

Fig. 9 Methane activation by oxidative addition over (phen)Ir(Bpin)$_3$

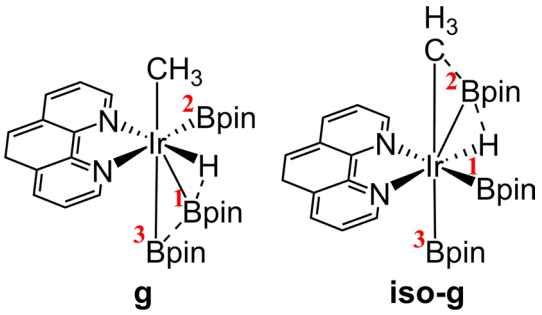

Fig. 10 The possible products of oxidative addition: (**g**) seven-coordinated (phen)Ir(H)(methyl)(Bpin)$_3$ complex; (**iso-g**) its isomer. Dotted lines indicate partial bonds; numbers in red are for identifying Bpin groups

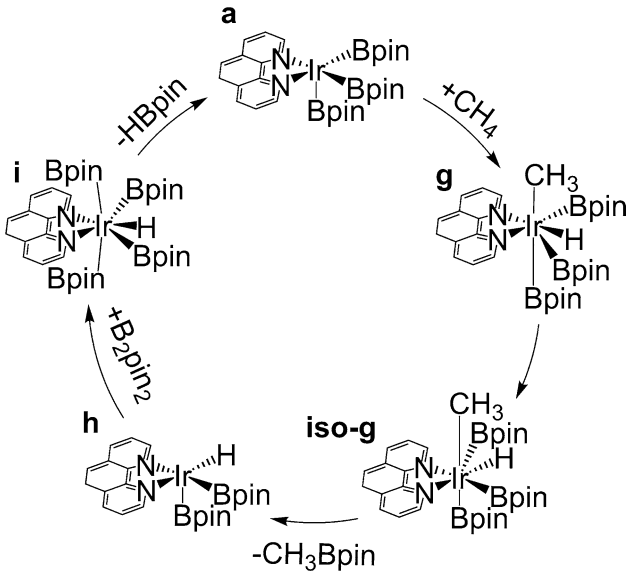

Fig. 11 Energetically most favorable catalytic cycle for CH_4 borylation over the (phen)Ir(Bpin)$_3$ complex

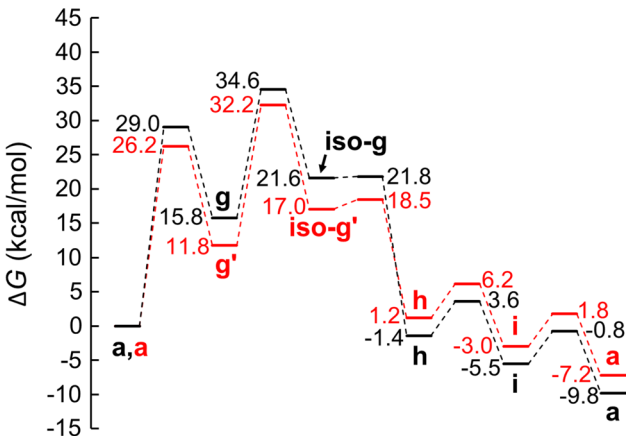

Fig. 12 Gibbs free energy profiles for catalytic CH_4 (black) and CH_3Bpin (red) borylation reactions over complex **a**. Corresponding free energy (kcal/mol) is shown beside each intermediate and was calculated using the M06-L functional [33] as implemented in the *Gaussian 16* program [32]. The methyl groups in **g** and **iso-g** become –CH_2Bpin groups in complex **g′** and **iso-g′**

indicating low catalytic activity for the borylation reaction. We conclude that complex **a** is the dominant active species of the Ir catalyst supported on UiO-67.

3.2.4 Borylation mechanism and isomerization of the Ir(V) complex

Figure 11 shows the energetically most favorable catalytic cycle for methane borylation to produce monoborylated methane (CH_3Bpin). The corresponding free energy profile is given in Fig. 12 (in black). This catalytic cycle involves five reaction steps, and it agrees with the reaction mechanism proposed by other research groups [18, 19] for the homogeneous catalyst in having the following steps: (1) C–H bond activation through oxidative addition to produce seven-coordinated **g**; (2) isomerization of **g** to **iso-g**; (3) formation of the main product (CH_3Bpin); (4) activation of the B_2pin_2 molecule; and (5) catalyst regeneration accompanied by the formation of the HBpin byproduct. According to our calculations, the C–H bond activation (oxidative addition) step has the highest free energy of activation (29.0 kcal/mol) of any step and is in good agreement with the free energies of activation reported by Smith et al. [18] (31.4 kcal/mol) and Ahn et al. [19] (35.4 kcal/mol) for the homogeneous mechanism.

We then computed the overall free energy of activation for methane borylation, where overall free energy of activation is defined as the free energy span in the energetic span model as reviewed by Kozuch and Shaik [41]. This requires determining the turnover-determining intermediate (TDI) and the turnover-determining transition state (TDTS). The TDI is the intermediate which if chosen as the starting point of the catalytic cycle, will give the highest free energy span along one complete forward cycle which returns to the TDI; and the transition state producing this free energy span is defined as the TDTS. For the catalytic cycle in Fig. 11 and the black profile of Fig. 12, the TDI is determined as intermediate **a**, the TDTS is the transition state that connects intermediate **g** and **iso-g**, and the overall free energy

of activation (the highest free energy span) for generating CH_3Bpin is 34.6 kcal/mol.

The overall free energies of activation were computed with the same procedure for other explored catalytic cycles. Details regarding the other explored reaction cycles are provided in the ESM. Our results show that other explored catalytic cycles exhibit higher than 34.6 kcal/mol overall free energies of activation. We conclude that the turnover-determining transition state is that corresponding to isomerization after the C–H bond activation in Figs. 11 and 12, and this state cannot be avoided.

The analogous reaction steps are now considered for the borylation of the CH_3Bpin molecule to produce CH_2Bpin_2. The associated energy profile is provided as the red profile in Fig. 12. The prime symbol for intermediates **g′** and **iso-g′** denotes that the methyl group in the corresponding intermediates **g** and **iso-g** is replaced with a $-CH_2Bpin$ group. Based on the energetic span model, the overall free energy of activation is 32.2 kcal/mol with intermediate **a** again being the TDI and the transition state that connects intermediate **g′** and **iso-g′** being the TDTS. The slightly lower overall barrier indicates that the diborylated methane is an energetically more favorable product than CH_3Bpin. Therefore, we conclude that the experimentally observed chemoselectivity toward the CH_3Bpin is not due to the electronic effect of either the UiO-67 framework or the Ir reactive center, and is most likely due to the UiO-67 framework confinement on CH_3Bpin and CH_2Bpin_2 transport that we discussed earlier in the subsection on steric effects.

The implicit inclusion of solvent effect with *n*-dodecane as the solvent slightly increases the overall activation energy but does not change the reaction mechanism. The overall free energy of activation becomes 35.7 and 35.4 kcal/mol for producing CH_3Bpin and CH_2Bpin_2, respectively.

The isomerization of complex **g** to give **iso-g** was further examined through the DDEC6 [42] bond order analysis. This analysis shows that the relatively high barrier associated with the isomerization step between complex **g** and **iso-g** is caused by the breaking and forming of partial bonds between the hydride and the Bpin groups near the Ir atom. The computed bond orders and bond lengths of selected bonds of **g** and **iso-g** are summarized in Table 4. According to the DDEC6 bond order analysis, averaging the results over **g** and **iso-g**, the sum of bond orders (SBO) is 5.1 for the Ir atom, 3.5 for B and N atoms, 1.1 for the hydride, and 3.9 for the C atom in methyl. For complex **g**, the bond order between the hydride and the B atom in the first Bpin group (Fig. 10) is 0.21, which is reduced to 0.02 in **iso-g**. On the other hand, the bond order between the hydride and the B atom in the second Bpin group increases from 0.03 in **g** to 0.23 in **iso-g**. We also found B–B bond breaking and C–B bond forming. The bond order between the B atoms of the first and third Bpin decreases from 0.23 in **g** to 0.06 in **iso-g,** and the bond order between the C in methyl and the B in the second Bpin increases from 0.04 in **g** to 0.12 in **iso-g**. Optimized geometries and DDEC outputs for complexes **g** and **iso-g** are provided in the ESM.

Table 4 Computed bond lengths (*L*, Å) and DDEC6 bond orders (BO) of selected atom pairs in complexes (**g**) and (**iso-g**)

	g		**iso-g**	
	L	BO	L	BO
H–B(1)	1.66	0.21	2.51	0.02
H–B(2)	2.37	0.03	1.59	0.23
H–B(3)	3.10	0.00	2.26	0.05
B(1)–B(2)	2.91	0.02	2.83	0.03
B(1)–B(3)	2.12	0.23	2.63	0.06
B(2)–B(3)	2.98	0.02	3.66	0.00
C–H	2.65	0.02	3.33	0.00
C–B(1)	3.99	0.00	3.08	0.02
C–B(2)	2.88	0.04	2.45	0.12

"C" denotes the C atom in the methyl group, "H" denotes the hydride, and B(*n*) (*n* = 1, 2, 3) denotes the B atom in Bpin groups as numbered in Fig. 10

3.2.5 Further analyses of the chemoselectivity of the Ir-decorated UiO-67 catalyst

As noted in the earlier steric effect subsection, the CH_2Bpin_2 molecule can be dissociated into CH_2Bpin and Bpin groups by the tethered Ir reaction center to free up the diffusion path of the framework. This process corresponds to the step to go from complex **h** to **iso-g′** as shown in the red profile of Fig. 12 with a free energy of activation of 17.3 kcal/mol. The corresponding electronic activation barrier (see Computational Methods) for this step (**h** → **iso-g′**) is 16.5 kcal/mol and is smaller than that for CH_2Bpin_2 diffusion in model tpm-UiO-67-Ir which is 24.7 kcal/mol, as presented in the earlier paragraph. Furthermore, as shown in Fig. 5, the CH_2Bpin_2 molecule energetically prefers to reside at position 5 of Fig. 4, which corresponds to the closest distance between the Ir center and the CH_2Bpin_2 molecule, while it moves along the diffusion pathway and therefore increases the possibility for the CH_2Bpin_2 molecule to react with the Ir center.

The competition between diffusion and possible reverse reaction of CH_2Bpin_2 may be further analyzed as follows: To reverse the diborylation reaction by following the red profile of Fig. 12 from right to left, an overall free energy of activation of 39.4 kcal/mol is required with intermediate **a** on the right-hand side of Fig. 12 as TDI and the transition state that connects intermediate **g′** and **iso-g′** as TDTS. In comparison, generating CH_3Bpin through CH_4 borylation by following the black profile of Fig. 12 from left to right,

requires an overall free energy of activation of 34.6 kcal/mol with intermediate **a** on the left-hand side of Fig. 12 as TDI and the transition state that connects intermediate **g** and **iso-g** as TDTS.

The result of the previous paragraph may be compared to that for the octahedral complexes. In particular, when we applied the octahedral model **oct-a** instead of complex **a** as the catalyst for the reverse diborylation reaction and followed the right-to-left reaction mechanism in the red profile of Fig. 12, we found an overall activation barrier of 38.9 kcal/mol with **oct-a** as TDI and the corresponding transition state that connects intermediate **oct-g′** and **oct-iso-g′** as TDTS. In comparison, using complex **oct-a** for CH_4 borylation and following the reaction mechanism as going from left to right in the black profile of Fig. 12, require an overall activation barrier of 42.8 kcal/mol with **oct-a** as TDI and the transition state that connects intermediate **oct-g** and **oct-iso-g** as TDTS.

Octahedral models with more Ir sites are not evaluated in this study because (1) even though having more than one Ir site in an octahedral cage could potentially impose more steric congestion at the active site, it would also require a higher activation barrier for the C–H bond activation of CH_3Bpin to happen, and the **oct-a** complex with one Ir site will become the more energetically favorable reaction site, and (2) even though the experimentally reported UiO-67-Mix-Ir catalyst has higher concentration of Ir sites on average [5], uneven distribution of the Ir atoms within the framework should allow at least some low-Ir-concentration areas where only one Ir atom per one octahedral cage is possible. Therefore, the C–H bond activation of CH_3Bpin through oxidative addition to give Ir–hydride and Ir–CH_2Bpin was examined using the octahedral complex **oct-a**, which contains one Ir active site in one octahedral cage of the framework, and in the next paragraph we will use this model to consider the possibility of having the reaction pathway of reaction R2 (diborylation reaction) blocked due to the steric confinement of the modified UiO-67 framework, which is another possible cause for the experimentally observed chemoselectivity of the UiO-67-supported Ir catalyst. However, our calculations do not show any evidence for such steric confinement effect of the framework at the Ir center.

Considering that reaction R2 utilizes CH_3Bpin as a reactant to produce CH_2Bpin_2, and that CH_3Bpin was generated at the Ir active center and can diffuse within and out the framework under the experimental conditions [5], we believe that the CH_3Bpin molecule can easily reach and react with the Ir active center for the diborylation reaction (R2). The C–H bond activation of the methyl group in CH_3Bpin using **oct-a** was calculated, and the corresponding reaction energy and activation barrier are, respectively, 3.4 and 11.5 kcal/mol. The same C–H bond activation step over the homogeneous Ir catalyst (complex **a**) gives an electronic reaction energy of 3.9 kcal/mol and an electronic activation barrier of 16.1 kcal/mol. Therefore, we conclude that the steric confinement of UiO-67 does not inhibit the C–H bond activation reaction.

As mentioned earlier, we also considered using **oct-a** as the catalyst for both CH_4 borylation and diborylation reactions. For the CH_4 borylation reaction we obtained an overall activation barrier of 42.8 kcal/mol. For the diborylation reaction (following the reaction mechanism as going from left to right in red profile of Fig. 12), we obtained an overall activation barrier of 33.5 kcal/mol with **oct-a** as TDI and the corresponding transition state that connects intermediate **oct-g′** and **oct-iso-g′** as TDTS. The barrier difference between CH_4 borylation and diborylation reactions using **oct-a** as the catalyst further suggests that the UiO-67-supported Ir catalyst tends to give CH_2Bpin_2 as the energetically more favored product and that the chemoselectivity of the catalyst toward CH_3Bpin comes from the effect of steric confinement of the framework on the product diffusion process.

4 Summary and concluding remarks

Confinement effects are often invoked as a feature that can increase selectivity in catalysis by nanoporous materials [43], but understanding the origin of the confinement effect in detail is rare. In this study, we employed density functional calculations on model Ir(III) catalysts in an effort to probe the overall mechanism of methane borylation and to interpret recent experimental evidence for high chemoselectivity of the metal–organic framework-supported iridium catalyst toward monoborylated methane instead of the undesired over-borylated product, diborylated methane.

Our calculations indicate that the energetic barrier for the formation of diborylated methane is actually lower than that for monoborylated methane. The Ir(III) with three binding pinacolborane ligands is identified as the most energetically favorable active species for methane borylation within the UiO-67-supported Ir catalytic system. Our mechanistic study performed using the $(phen)Ir(Bpin)_3$ complex, after validating that the electronic effect of the framework is negligible, yielded an overall free energy of activation for methane borylation over $(phen)Ir(Bpin)_3$ of 34.6 kcal/mol, which is 2.4 kcal/mol higher than that of the CH_3Bpin borylation to give CH_2Bpin_2 and which makes the CH_2Bpin_2 the energetically more favorable product. Our calculation also shows that in contrast to common assumptions [18, 19], the isomerization of seven-coordinated Ir(V) complex, instead of the methane activation through oxidative addition, is the turnover-limiting step in the catalytic methane borylation. The relatively large barrier associated with the isomerization reaction comes

from the breaking and forming of partial bonds between the hydride and Bpin ligands around the Ir center.

Our results thus imply that the high selectivity of UiO-67-supported Ir borylation catalyst toward CH_3Bpin solely comes from the inhibited transportation of the CH_2Bpin_2 molecule; that is, the steric confinement effect of MOF UiO-67 is a beyond-the-active-site effect arising solely from the UiO-67 framework inhibiting the migration of borylated methane molecules within the MOF. Barriers of 10.5 and 24.7 kcal/mol were estimated for, respectively, moving CH_3Bpin and CH_2Bpin_2 between pores inside modified UiO-67 with coordinated $Ir(Bpin)_3$ complex. Having computed a low barrier for diffusion for the monoborylated product and a high barrier for diffusion of the diborylated product, we conclude that monoborylated methane, once formed, can easily interact with the catalyst to readily form diborylated methane. However, the much larger diborylated product diffuses very slowly through the MOF. This product is suggested to remain near the catalyst where it can decompose into the monoborylated product. Thus, the chemoselectivity of the catalysis comes from the effect of steric confinement of the framework on the product diffusion rate.

We also considered the possibilities in which the UiO-67 framework obstructs the borylation reaction over the Ir active site. However, our results do not support this assumption with the model systems we used. Our conclusions are not in full agreement with experiment because the experiment showed no production CH_2Bpin_2 rather than just a reduced yield. More detailed analysis, both computationally and experimentally, on the local structure of the UiO-67-Mix-Ir catalyst could shed more light on the nature of the steric confinement effect of the UiO-67 MOF. It would be particularly interesting to study the effect of varying the loading.

Acknowledgements The authors are grateful to Massimiliano Delferro, Omar K. Farha, and Connie C. Lu for many helpful discussions. This work was supported as part of the Inorganometallic Catalysis Design Center, an Energy Frontier Research Center funded by the U.S. Department of Energy, Office of Science, Basic Energy Sciences under Award DE-SC0012702.

Data Availability Cartesian coordinates for all optimized models and complexes (in XYZ file format) and for periodic structures (in CIF file format), and DDEC bond order analysis outputs for complexes **g** and **iso-g** are provided in the OUTPUT file which may be opened as a text file. Detailed energy profiles for CH_3Bpin and CH_2Bpin diffusion in UiO-67 and for catalytic methane borylation cycles over the (phen) $Ir(Bpin)_3$ complex, and verifications of the *CP2K* results are provided in the ESM file.

Compliance with ethical standards

Conflict interest The authors declare that there is no competing interest.

References

1. Cook AK, Schimler SD, Matzger AJ, Sanford MS (2016) Catalyst-controlled selectivity in the C–H borylation of methane and ethane. Science 351:1421–1424
2. Crabtree RH, Lei A (2017) Introduction: CH activation. Chem Rev 117:8481–8482
3. Gunsalus NJ, Koppaka A, Park SH, Bischof SM, Hashiguchi BG, Periana RA (2017) Homogeneous functionalization of methane. Chem Rev 117:8521–8573
4. Hartwig J (2016) Evolution of C–H bond functionalization from methane to methodology. J Am Chem Soc 138:2–24
5. Zhang X, Huang Z, Ferrandon M, Yang D, Robison L, Li P, Wang TC, Delferro M, Farha OK (2018) Catalytic chemoselective functionalization of methane in a metal–organic framework. Nat Catal 1:356–362
6. Cho S-H, Ma B, Nguyen ST, Hupp JT, Albrecht-Schmitt TEA (2006) A metal–organic framework material that functions as an enantioselective catalyst for olefin epoxidation. Chem Commun 37(24):2563–2565
7. Guo Z, Xiao C, Maligal-Ganesh RV, Zhou L, Goh TW, Li X, Tesfagaber D, Thiel A, Huang W (2014) Pt nanoclusters confined within metal–organic framework cavities for chemoselective cinnamaldehyde hydrogenation. ACS Catal 4:1340–1348
8. Madrahimov ST, Gallagher JR, Zhang G, Meinhart Z, Garibay SJ, Delferro M, Miller JT, Farha OK, Hupp JT, Nguyen ST (2015) Gas-phase dimerization of ethylene under mild conditions catalyzed by MOF materials containing (bpy)Ni^{II} complexes. ACS Catal 5:6713–6718
9. Ye R, Hurlburt TJ, Sabyrov K, Alayoglu S, Somorjai GA (2016) Molecular catalysis science: perspective on unifying the fields of catalysis. Proc Natl Acad Sci 113:5159–5166
10. Metzger ED, Comito RJ, Hendon CH, Dincă M (2017) Mechanism of single-site molecule-like catalytic ethylene dimerization in Ni-MFU-4. J Am Chem Soc 139:757–762
11. Ali-Mousa H, Amador RN, Martinez J, Lamaty F, Carboni M, Bantreil X (2017) Synthesis and post-synthetic modification of UiO-67 type metal–organic frameworks by mechanochemistry. Mater Lett 197:171–174
12. Hu Z, Zhao D (2017) Metal–organic frameworks with lewis acidity: synthesis, characterization, and catalytic applications. CrystEngComm 19:4066–4081
13. Kumar G, Das SK (2017) Coordination frameworks containing compounds as catalysts. Inorg Chem Front 4:202–233
14. Rogge SMJ, Bavykina A, Hajek J, Garcia H, Olivos-Suarez AI, Sepúlveda-Escribano A, Vimont A, Clet G, Bazin P, Kapteijn F, Daturi M, Ramos-Fernandez EV, Llabrés i Xamena FX, Van Speybroeck V, Gascon J (2017) Metal–organic and covalent organic frameworks as single-site catalysts. Chem Soc Rev 46:3134–3184
15. Bernales V, Ortuño MA, Truhlar DG, Cramer CJ, Gagliardi L (2018) Computational design of functionalized metal–organic frameworks nodes for catalysis. ACS Cent Sci 4:5–19
16. Xu W, Thapa KB, Ju Q, Fang Z, Huang W (2018) Heterogeneous catalysts based on mesoporous metal–organic frameworks. Coord Chem Rev 373:199–232
17. Wang C, An B, Lin W (2019) Metal–organic frameworks in solid–gas phase catalysis. ACS Catal 9:130–146
18. Smith KT, Berritt S, González-Moreiras M, Ahn S, Smith MR, Baik M-H, Mindiola DJ (2016) Catalytic borylation of methane. Science 351:1424–1427
19. Ahn S, Sorsche D, Berritt S, Gau MR, Mindiola DJ, Baik M-H (2018) Rational design of a catalyst for the selective monoborylation of methane. ACS Catal 8:10021–10031

20. Marenich AV, Cramer CJ, Truhlar DG (2009) Universal solvation model based on solute electron density and a continuum model of the solvent defined by the bulk dielectric constant and atomic surface tensions. J Phys Chem B 113:6378–6396
21. Kresse G, Hafner J (1993) Ab initio molecular dynamics for liquid metals. Phys Rev B 47:558–561
22. Kresse G, Hafner J (1994) Ab initio molecular-dynamics simulation of the liquid–metal–amorphous–semiconductor transition in germanium. Phys Rev B 49:14251–14269
23. Kresse G, Furthmüller J (1996) Efficiency of ab initio total energy calculations for metals and semiconductors using a plane-wave basis set. Comput Mater Sci 6:15–50
24. Kresse G, Furthmüller J (1996) Efficient iterative schemes for ab initio total-energy calculations using a plane-wave basis set. Phys Rev B 54:11169–11186
25. Perdew JP, Ruzsinszky A, Csonka GI, Vydrov OA, Scuseria GE, Constantin LA, Zhou X, Burke K (2008) Restoring the density-gradient expansion for exchange in solids and surfaces. Phys Rev Lett 100:136406
26. Blöchl PE (1994) Projector augmented-wave method. Phys Rev B 50:17953–17979
27. Øien S, Wragg D, Reinsch H, Svelle S, Bordiga S, Lamberti C, Lillerud KP (2014) Detailed structure analysis of atomic positions and defects in zirconium metal–organic frameworks. Cryst Growth Des 14:5370–5372
28. Hutter J, Iannuzzi M, Schiffmann F, VandeVondele J (2014) CP2K: atomistic simulations of condensed matter systems. Wiley Interdiscip Rev Comput Mol Sci 4:15–25
29. Perdew J, Burke K, Ernzerhof M (1996) Generalized gradient approximation made simple. Phys Rev Lett 77:3865–3868
30. Goedecker S, Teter M, Hutter J (1996) Separable dual-space Gaussian pseudopotentials. Phys Rev B 54:1703–1710
31. Grimme S, Antony J, Ehrlich S, Krieg H (2010) A consistent and accurate ab initio parametrization of density functional dispersion correction (DFT-D) for the 94 elements H-Pu. J Chem Phys 132:154104
32. Frisch MJ, Trucks GW, Schlegel HB, Scuseria GE, Robb MA, Cheeseman JR, Scalmani G, Barone V, Petersson GA, Nakatsuji H, Li X, Caricato M, Marenich AV, Bloino J, Janesko BG, Gomperts R, Mennucci B, Hratchian HP, Ortiz JV, Izmaylov AF, Sonnenberg JL, Williams-Young D, Ding F, Lipparini F, Egidi F, Goings J, Peng B, Petrone A, Henderson T, Ranasinghe D, Zakrzewski VG, Gao J, Rega N, Zheng G, Liang W, Hada M, Ehara M, Toyota K, Fukuda R, Hasegawa J, Ishida M, Nakajima T, Honda Y, Kitao O, Nakai H, Vreven T, Throssell K, Montgomery JA Jr, Peralta JE, Ogliaro F, Bearpark MJ, Heyd JJ, Brothers EN, Kudin KN, Staroverov VN, Keith TA, Kobayashi R, Normand J, Raghavachari K, Rendell AP, Burant JC, Iyengar SS, Tomasi J, Cossi M, Millam JM, Klene M, Adamo C, Cammi R, Ochterski JW, Martin RL, Morokuma K, Farkas O, Foresman JB, Fox DJ (2016) Gaussian 16 (revision A.03). Gaussian Inc, Wallingford
33. Zhao Y, Truhlar DG (2006) A new local density functional for main-group thermochemistry, transition metal bonding, thermochemical kinetics, and noncovalent interactions. J Chem Phys 125:194101
34. Cramer CJ, Truhlar DG (2009) Density functional theory for transition metals and transition metal chemistry. Phys Chem Chem Phys 11:10757–10816
35. Yu HS, He X, Truhlar DG (2016) MN15-L: a new local exchange-correlation functional for kohn–sham density functional theory with broad accuracy for atoms, molecules, and solids. J Chem Theory Comput 12:1280–1293
36. Weigend F (2006) Accurate coulomb-fitting basis sets for H to Rn. Phys Chem Chem Phys 8:1057–1065
37. Weigend F, Ahlrichs R (2005) Balanced basis sets of split valence, triple zeta valence and quadruple zeta valence quality for H to Rn: design and assessment of accuracy. Phys Chem Chem Phys 7:3297–3305
38. Yu HS, Fiedler LJ, Alecu IM, Truhlar DG (2017) Computational thermochemistry: automated generation of scale factors for vibrational frequencies calculated by electronic structure model chemistries. Comput Phys Commun 210:132–138
39. Pratt LM, Truhlar DG, Cramer CJ, Kass SR, Thompson JD, Xidos JD (2007) Aggregation of alkyllithiums in tetrahydrofuran. J Org Chem 72:2962–2966
40. Marenich AV, Jerome C, Cramer CJ, Truhlar DG (2012) Charge model 5: an extension of hirshfeld population analysis for the accurate description of molecular interactions in gaseous and condensed phases. J Chem Theory Comput 8:527–541
41. Kozuch S, Shaik S (2011) How to conceptualize catalytic cycles? The energetic span model. Acc Chem Res 44:101–110
42. Manz TA (2017) Introducing DDEC6 atomic population analysis: part 3. Comprehensive method to compute bond orders. RSC Adv 7:45552–45581
43. Mouarrawis V, Plessius R, van der Vlugt JI, Reek JNH (2018) Confinement effects in catalysis using well-defined materials and cages. Front Chem 6:623